Construction and Building Materials 450 (2024) 138707

Contents lists available at ScienceDirect

Construction and Building Materials

journal homepage: www.elsevier.com/locate/conbuildmat

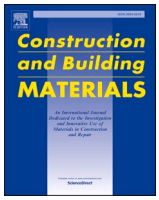

Innovative development of geopolymer-based lunar high strength concrete for sustainable extra-terrestrial construction using large-scale regolith simulants

Ruizhe Shao, Chengqing Wu *, Jun Li

School of Civil and Environmental Engineering, University of Technology, Sydney, NSW 2007, Australia

ARTICLE INFO

Keywords:
Lunar high strength concrete
Lunar soil simulant
In-situ resource utilization (ISRU)
Compression performance
Microstructure

ABSTRACT

The quest for viable construction materials for lunar bases has directed scientific inquiry towards the lunar in-situ resource utilization (ISRU), notably lunar regolith, to synthesize concrete. This study develops an innovative lunar high strength concrete (LHSC) utilizing lunar highlands simulant (LHS-1) and lunar mare simulant (LMS-1) as both precursors and aggregates within the concrete matrix. Mixtures were cured under the conditions simulating the lunar surface temperatures, enabling an evaluation of properties such as flowability, unit weight, compressive strength, modulus of elasticity, and microstructure patterns. Test results indicated that the LMS-1 mixtures exhibited a better flowability and higher unit weight as compared to LHS-1 counterparts. Moreover, the highest 28-day strength was 106.7 MPa and 98.7 MPa for LHS-1 and LMS-1 derived LHSC, respectively. Microstructure analysis revealed that under the identical simulant additions, LHS-1 mixes exhibited superior structural compactness with denser amorphous gels and fewer microcracks. In addition, it possessed a lower Si/Al ratio and diffraction peak of calcite, along with a greater Ca/Si ratio and hump intensity of amorphous gel phases. The development of this cement-free LHSC, incorporating up to 80 % large-scale lunar materials in the total binder mass, plays a critical role in advancing ISRU on the Moon, thus boosting the viability and sustainability of future lunar construction and habitation while significantly reducing transportation and fabrication costs.

1. Introduction

During the 1960s and 1970s, the National Aeronautics and Space Administration (NASA) of the United States orchestrated the Apollo Space Program, culminating in the historic achievement of human footprints on the Moon's surface in July 1969. As the first frontier in deep space exploration, the Moon offers opportunities for technology validation, life support system testing, and practical experience of the cosmic radiation environment, thereby laying the foundation for the further space journeys [1]. Through lunar exploration, the infrastructure establishment, and resource utilization, humanity can better deepen its comprehension of the solar system's inception and evolution, while simultaneously fortifying its technological and physiological readiness for the future expedition to remote celestial bodies [2].

Lunar construction, which refers to the development of infrastructural elements on the lunar surface, plays an integral role in advancing in-depth lunar research initiatives. Moreover, such construction is vital for devising protective measures to safeguard both personnel and facilities against the severe challenges of the lunar environment, such as vacuum conditions, extreme thermal variations, lunar dust, radiation exposure, and potential meteoroid impacts [3,4]. In formulating strategies for lunar construction development, a primary consideration is the selection of pivotal materials tailored for diverse infrastructure designs. Given that concrete is widely used in terrestrial construction owing to its remarkable compressive strength, excellent durability, and extensive strength gradations, its inherent stability and high reliability render it an optimal choice for lunar architectural ventures [5]. Given the substantial raw material requirements for concrete production, coupled with the significant logistical and financial challenges of transporting these materials from Earth to the Moon, leveraging lunar in-situ resource utilization (ISRU) for concrete production has emerged as a more economically and pragmatically feasible solution [6–8].

Lunar regolith is a fine-grained, fragmented layer on the moon's

* Corresponding author.
E-mail address: Chengqing.wu@uts.edu.au (C. Wu).

https://doi.org/10.1016/j.conbuildmat.2024.138707
Received 12 August 2024; Received in revised form 28 September 2024; Accepted 9 October 2024
Available online 18 October 2024
0950-0618/© 2024 The Author(s). Published by Elsevier Ltd. This is an open access article under the CC BY license (http://creativecommons.org/licenses/by/4.0/).

surface, consisting of the inorganic dust, rock fragments, and hit-induced glass beads, presenting opportunities for in-situ utilizations. Drawing from the comprehensive analyses of real lunar samples from global researchers (chemical and mineral attributes, particle distribution, maturation characteristics, and microscopic features [9–12]), lunar soil simulants have been meticulously engineered to emulate these properties to support a wide range of research and experimental endeavours on earth [13]. Currently, the prominent lunar regolith simulants used in academic research comprise the JSC-1a, MLS-1, LHS-1 and LMS-1 from the United States [8,14–16], FJS-1 and MKS-1 from Japan [17,18], CAS-1 and BH-1 from China [19,20], and KLS-1 from Korea [21]. The lunar concrete formulations include sulphur concrete, calcium sulphoaluminate cement concrete, vitrified regolith concrete, and geopolymer concrete. For instance, Toutanji et al. [16] studied the use of sulphur as an alternative binder (35 %) combined with the simulant JSC-1a as an aggregate utilization (65 %) in lunar concrete, evaluating its resilience to hypervelocity impacts and space radiation. It was indicated that this lunar sulphur concrete exhibited a normal compressive strength of 31 MPa and a faster setting time as compared to cement concrete, and the introduction of carbon and hydrogen offered potential radiation shielding benefits. Moreover, while NASA's hypervelocity impact model required additional data to enhance its precision, it still showcased potential for practical application. For another instance, Cai et al. [4] studied the impact of calcium hydroxide content and autoclaving parameters on lunar calcium sulphoaluminate cement concrete made with a basaltic lunar simulant from CAS-1. They found that incorporating $Ca(OH)_2$ and increasing calcium hydroxide content and briquetting pressure into the lunar concrete system enhanced its mechanical properties in comparison with the conventional clinker cement, but a finer simulant granularity compromised the mixture's compactness.

It is important to highlight that geopolymer concrete stands out as a promising construction material for lunar bases, attributed to its remarkable dimensional stability at high temperatures, freeze-thaw resistance, vacuum stability, radiation resistance, and low water consumption characteristics [2,22–24]. Geopolymer is synthesized via the chemical reaction of aluminosilicate source materials, such as natural minerals and industrial by-products, with an alkaline activator. During this process, water serves solely as a medium, facilitating the dissolution, transport, and polymerization of ions within the mixture, and it does not integrate into the final geopolymer matrix [25,26]. Hence, compared to cement concrete, geopolymer generally requires less water for optimal workability, and a portion of water can be recovered after geopolymer formation [27,28]. This characteristic is especially valuable on the moon, where the water resources are limited. Moreover, studies on lunar regolith reveal that it possesses abundant aluminosilicate elements crucial for geopolymer synthesis, which bolsters the prospects for ISRU in preparing geopolymer concrete and the subsequent lunar structures [6,13,29]. Alexiadis et al. [30] investigated the geopolymerization of the regolith simulant JSC-1a by preparing cylindrical specimens with varying concentrations of NaOH and K_2SiO_3. The findings showed that the geopolymerization readily produced a rock-like material, and it exhibited a higher compressive strength (18.4 MPa) than cement-based concrete (12.6 MPa) owning to the simulant's heightened reactivity. Zhou et al. [31] synthesized lunar geopolymers utilizing a novel lunar simulant named ground volcanic scoria to evaluate its potential for lunar construction applications. They discovered that the curing temperature, which varied between 20 °C and 80 °C, was the most important factor affecting the compressive strength of lunar geopolymers, and the mass ratio of NaOH to simulant played a predominant role in enhancing their flexural strength. The microstructural observations of the Si variation under varying conditions provided preliminary insights into the reaction mechanism of the synthesized geopolymers. In addition to the above research, Zhou et al. [7,20,32] likewise investigated the feasibility of preparing lunar geopolymers using BH-1 simulant and evaluated their mechanical and durability properties under lunar environments and carbon nano-fibre reinforcement. They found that the geopolymers exhibited an adequate early-age compressive strength of 38.2 MPa after being cured under lunar environments for 72 h, which corresponded to the 324–384 h of one lunar day. Moreover, evident temperature fluctuations between −180 °C and 100 °C negatively affected the geopolymer's mechanical and durability characteristics, with flexural strength declining by 70 % and the total porosity increasing by 11 %. Predictably, the inclusion of milled carbon nano-fibres demonstrated a prominent positive impact on enhancing the strength, toughness, and ductility of the lunar geopolymers, largely due to the nucleation and bridging benefits of the fibres.

Space exploration and lunar base construction are at the forefront of contemporary science, with a significant focus on using lunar resources to produce lunar concrete. However, the existing research is still in its infancy, and the resulting concrete underperforms across several properties, making it inadequate for long-term use against the extreme condition on the moon. This study aims to develop a novel cement-free geopolymer-based lunar high strength concrete (LHSC) by using two types of lunar soil simulants. The optimum mass percentage between the soil simulants and other precursors was identified by balancing the economic efficiency with compression properties of the synthesized LHSC. In addition, Scanning Electron Microscope (SEM), Energy Dispersive X-ray Spectroscopy (EDS), and X-ray Diffraction (XRD) analyses were utilized to study the microstructural morphology of various geopolymer mixtures. The use of ISRU in the production of LHSC promises a sustainable method for future lunar constructions, offering a novel solution to logistical and economic challenges of extra-terrestrial construction and deep space exploration.

2. Experimental program

2.1. Raw materials and mix proportion

The lunar regolith simulants utilized to prepare LHSC were LHS-1 and LMS-1, both developed by the Space Resource Technologies (SRT) Exolith Lab. The particle size for LHS-1 ranged from 0.04 to 1000 μm with a median diameter of 98 μm, while for LMS-1, it ranged from 0.04 to 300 μm with a median size of 45 μm. The morphology of both simulants displayed angular shapes aimed to mimic the abrasive nature of lunar dust, and they were optimized for flowability and performance utilizing grinding and sieving to closely match lunar dust behaviour [8]. The uncompressed bulk density of LHS-1 and LMS-1 was 1.27 and 1.56 g/cm^3, respectively, which were attributed to the variations in their mineral composition and particle size distribution. Table 1 lists the main oxide compositions of LHS-1 and LMS-1, as measured by Exolith Lab, alongside the corresponding compositions of the actual highlands, mare, and the Apollo 17 landing site regolith, referenced in the literatures [31,33]. In addition to the simulants, the earth-sourced materials such as ground granulated blast-furnace slag (GGBS), silica fume, and Class F fly ash were selected as precursor components for the geopolymer binders. Their major compositions and physical parameters are detailed in Table 2, and the powdery appearance of the introduced solid materials is shown in Fig. 1. Additionally, 99.0 % pure NaOH and Na_2SiO_3 powder

Table 1
Chemical compositions of LHS-1, LMS-1, lunar highlands, mare and Apollo 17 sites regolith (wt%).

Source material	SiO_2	Al_2O_3	CaO	FeO/ Fe_2O_3	MgO	TiO_2	P_2O_5
LHS−1	49.1	26.3	13.5	3.2	2.9	0.6	0.2
LMS−1	40.2	14.0	9.8	13.9	12.0	7.3	1.0
Highlands regolith	45.0	25.1	14.9	6.3	7.6	0.5	0.1
Mare regolith	41.0	12.4	11.4	16.6	8.9	8.5	0.1
Apollo 17 regolith	45.1	27.3	15.7	5.1	5.7	0.5	0.1

Table 2
Chemical compositions and physical parameters of geopolymer precursors.

Precursors	Chemical compositions (wt%)	Specific gravity	Bulk density (kg/m^3)	Fineness (m^2/kg)	LOI (%)
GGBS	CaO (43.6), SiO_2 (35.4), Al_2O_3 (10.8)	2.81	1275	395	0.48
Fly ash	SiO_2 (67.9), Al_2O_3 (23.8), Fe_2O_3 (6.3)	2.42	1041	430	1.20
Silica fume	SiO_2 (89.6), CaO (1.9), K_2O (1.3)	2.23	625	16,000	3.80

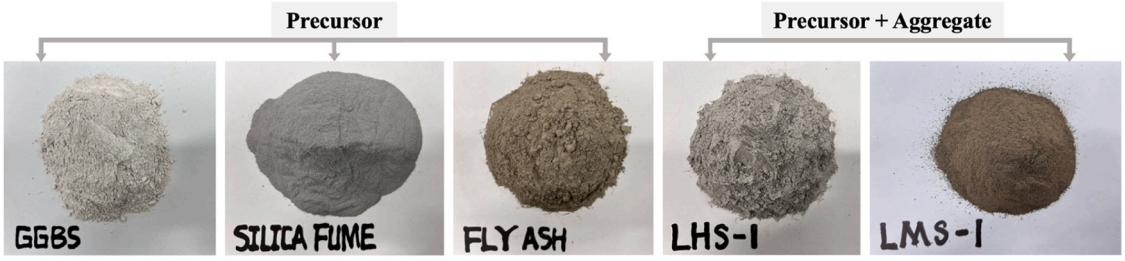

Fig. 1. Appearances of major raw materials of GGBS, silica fume, fly ash, and lunar regolith simulants.

with a modulus of 3.0 was utilized as the alkaline activator to establish a conductive alkaline environment for the hydration of binding materials. It is noteworthy that the addition of both simulants can act as both precursors and inactive fillers (functioning like concrete aggregates) during the geopolymerization process, attributed to their distinctive composition of aluminosilicate minerals (plagioclase feldspar, pyroxene, and olivine) as well as a granular appearance that closely resembles traditional concrete aggregates.

Table 3 exhibits the detailed mixture proportions of all the studied LHSC. To differentiate between the regolith simulants and the synthesized lunar concrete, the LHSC has been categorized into two groups: Lunar Highlands Simulant Concrete (LHiS-C) and Lunar Mare Simulant Concrete (LMaS-C). Within each group, the content of simulant was varied to explore its impact on the behaviour of LHSC. For instance, LC-HiS40 designates a lunar concrete with highlands simulant constituting 40 % of the total mass of precursors and aggregates (simulant + GGBS + silica fume + fly ash), while LC-MaS60 denotes a mix with mare simulant comprising 60 % of the total mass. It should be noted that the alkali activator solution (AAS), a blend of Na_2SiO_3 solution and NaOH powder, was pre-prepared in advance of the mixture's final mixing process. Moreover, given that the mass of AAS incorporated into each mixture was predetermined [34], the mix proportion of the AAS was set to a fiducial value. The ratio of the other components was adjusted based on the varying inclusions of the soil simulant, ensuring the mass ratio of solid materials to AAS to water remained at 3.96:1.00:0.13.

Table 3
Relative proportions of precursors/aggregates and water to AAS in studied LHSC.

Group	Sample	Simulant	GGBS	Silica fume	Fly ash	AAS	Water
LHiS-C	LC-HiS20	0.79	2.52	0.25	0.40	1.00	0.13
	LC-HiS40	1.58	1.89	0.19	0.30	1.00	0.13
	LC-HiS60	2.38	1.26	0.13	0.20	1.00	0.13
	LC-HiS80	3.17	0.63	0.06	0.10	1.00	0.13
LMaS-C	LC-MaS20	0.79	2.52	0.25	0.40	1.00	0.13
	LC-MaS40	1.58	1.89	0.19	0.30	1.00	0.13
	LC-MaS60	2.38	1.26	0.13	0.20	1.00	0.13
	LC-MaS80	3.17	0.63	0.06	0.10	1.00	0.13

2.2. Mixing and preparation

For the formulation of the developed LHSC mixtures, initial dry components like GGBS, silica fume, fly ash, and lunar simulants (LHS-1/LHiS and LMS-1/LMaS) were combined in a mixer until they exhibited a uniform state, a process lasting 4–7 min. The pre-blended AAS was then introduced to this blend, with the remaining water added during continuous mixing. The mixture's appearance was observed during this process to maintain good workability. Once the mixture was homogeneous, cubes in the dimension of 50 mm × 50 mm × 50 mm were cast utilizing a vibration table, ensuring minimal air pockets and irregularities within the mixture. As shown in Table 1, the compositions of the adopted LHS-1 simulant were strikingly similar to the lunar regolith from the Apollo 17 landing site, located near the 30° lower latitude [35]. Given this resemblance, this lunar environment was established as the standard for curing the LHSC. In the research conducted by Zhou et al. [7], it was indicated that the highest mechanical strength could be obtained by curing at temperatures of 93.0 °C for 0–12 h, 96.3 °C for 12–24 h, 97.9 °C for 24–36 h, and 99.6 °C for 36–48 h, aligning with the 324–372 h duration of one lunar day at 30° latitude. Therefore, the curing regime for the developed LHSC in this study was set to this 48 h timeframe with an average temperature of 96.7 °C. It is noteworthy that the vacuum conditions of the Moon were not considered in the curing process of hardened LHSC, as no adverse effects on lunar geopolymers were noted. This was attributed to reduced efflorescence characteristics as compared to those observed in an atmospheric environment [7]. Fig. 2 displays the representative LHSC samples after demoulding, incorporating both LHS-1 and LMS-1 in various contents. It should be noticed that the cubes with a 20–60 % simulant addition display a darker green hue, a characteristic that may be attributed to their more sufficient geopolymerization.

2.3. Testing methods

The performance of the synthesized lunar concrete was systematically evaluated via examining its flowability, unit weight, compression behaviour, and microstructural morphology. Flowability test was performed on the freshly prepared geopolymer mixtures in accordance with ASTM C1437 [36], immediately after the mixing. The uniaxial compression test, as per ASTM C109/C109M [37], was then conducted on hardened mixtures at 3, 7, and 28 days utilizing a 50-ton servo-hydraulic testing machine. The loading rate was 0.1 mm/min. In

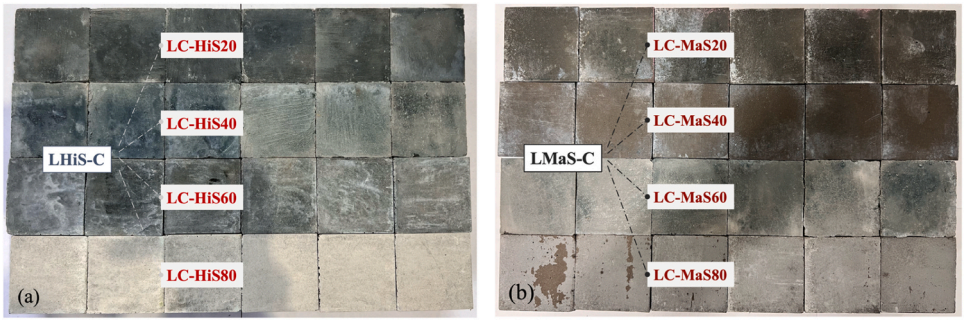

Fig. 2. Typical geopolymer-based lunar (a) highlands and (b) mare concrete samples after demoulding.

addition, to minimize the possibility of test errors, three identical samples from each mix were examined, and their average was recorded as the final value. It should be pointed out that the compression test was performed in unison with a digital image correlation (DIC) device, potentially assisting in capturing the failure progression and detailing the strain distribution across the shooting area. Fig. 3 shows the varnished LHSC samples and the setup for compression test including DIC apparatus. As for the micromorphology of the developed LHSC, intact fragments and powdered samples from 28-day tests underwent scanning in SEM-EDS systems and subjected to semi-quantitative XRD with diffraction angles between 10° and 70°.

3. Results and discussion

3.1. Flowability

Fig. 4 depicts the typical slump flowability of the fresh lunar mixtures with varying mass ratios of lunar highlands and mare soil simulants. Alongside the flow measurement, a visual examination was conducted, confirming that all mixtures were uniform without segregation and bleeding. In addition, owing to the varying appearances of the simulants as shown in Fig. 1, the resulting lunar mixtures presented with a hue that was marginally light grey and dark brown. Fig. 5 exhibits the averages of the two flow diameter measurements along with the flowability percentage for geopolymers based on different lunar simulants. It can be clearly observed that the flowability of both lunar geopolymers was significantly influenced by the mixing ratio of precursors and simulants. For example, the flow diameter expanded from 176 mm to 219 mm (increased by 24.4 %) as the mass ratio of LHS-1 rose from 20 % to 80 %, and the flowability percentage raised from 74.3 % to 116.8 %. This enhancement was primarily attributed to decreasing the mix proportion of GGBS, characterized by the irregularly shaped particles and a high calcium content, which decelerated the hydration process, leading to a moderate setting rate and an improved mixture mobility [38,39]. Additionally, the LMS-1-derived geopolymers demonstrated better flowability in contrast with the LHS-1 counterparts when the same amount of the lunar simulants was incorporated. This enhanced flowability could be ascribed to two parallel factors: the lower calcium content in LMS-1, as shown in Table 1, and its significantly higher silica-aluminium ratio (Si/Al = 3.78) in comparison with LHS-1 (Si/Al = 1.92). These characteristics likely reduced the reactivity of LMS-1 in the geopolymerization reaction, resulting in a mixture with lower viscosity [7]. In general, a nearly linear enhancement in the flowability of the prepared LHSC mixtures was observed with increasing contents of both simulants, as evidenced by a high correlation coefficient ($R^2 > 0.99$).

3.2. Unit weight

The unit weight of LHSC derived from LHS-1 and LMS-1 was studied as illustrated in Fig. 6. The data reflect averages calculated from three cubic samples after 28-day curing, which were utilized in the subsequent analysis. It can be observed that as the mass addition of both simulants in the raw material increased, there was a corresponding enhancement in the unit weight of lunar concrete. For instance, the unit weight for LC-HiS20 and LC-MaS20 samples was approximately 2072 and 2125 kg/m^3, respectively, which increased to 2191 and 2245 kg/m^3, rendering a rise of 5.8 % and 5.7 %, when the corresponding simulants constituted to 80 % of the total mass. This phenomenon is mainly attributed to the improved flowability of the fresh mixture, as indicated above, leading to a superior compactness of hardened mixtures. Notably, with the identical simulant addition, LMS-1 synthesized geopolymers with a higher unit weight as compared to those derived from LHS-1. This difference is due to its better flowability and inherently greater bulk density of LMS-1 over LHS-1.

3.3. Compression performance

3.3.1. Compressive strength

The variations in compressive strength of lunar geopolymers synthesized using LHS-1 and LMS-1 with varying proportions of simulant contents are displayed in Fig. 7. The inclusion of error bars on each data point represents the standard deviation, illustrating the consistency and variability of the experimental setup. For both simulants, a clear trend

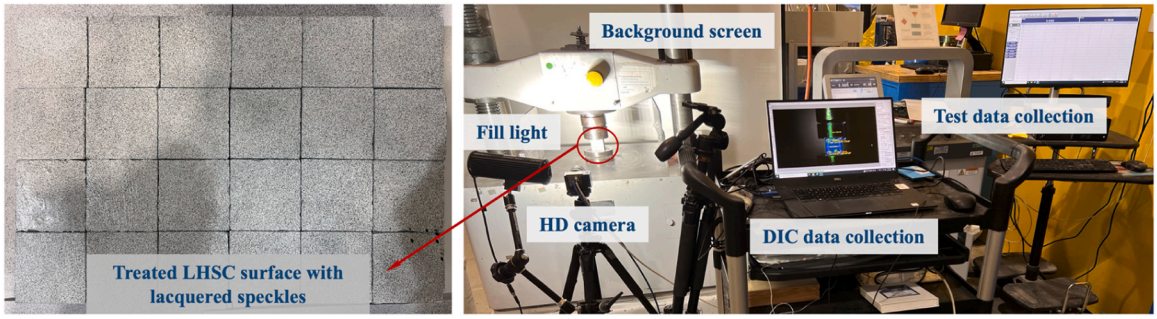

Fig. 3. Typical treated LHSC samples with lacquered speckles and the compression test setup.

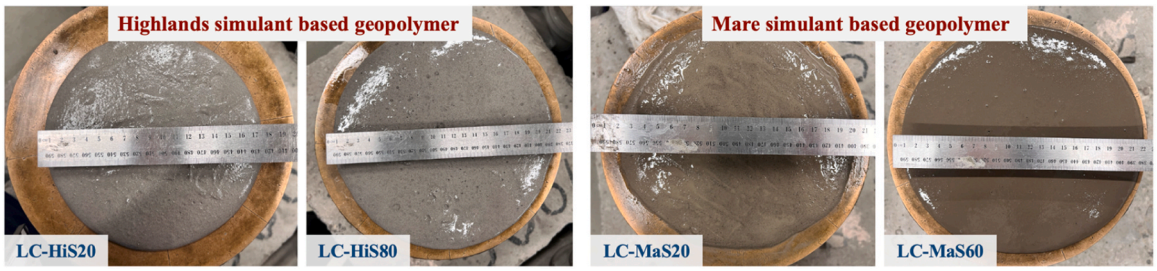

Fig. 4. Typical slump flowability of fresh LHS-1- and LMS-1- based lunar concrete mixtures.

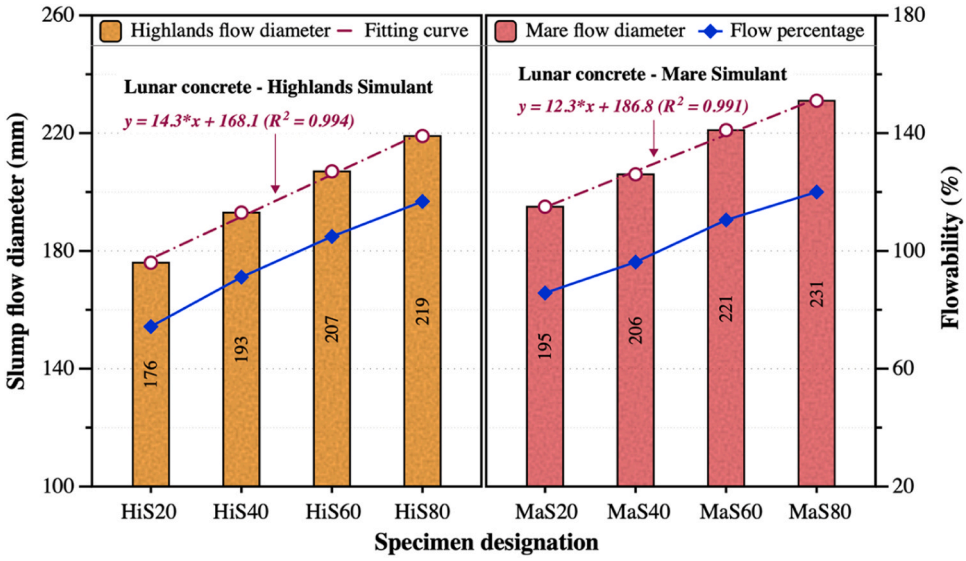

Fig. 5. Effect of regolith simulant addition on slump flowability of LHSC.

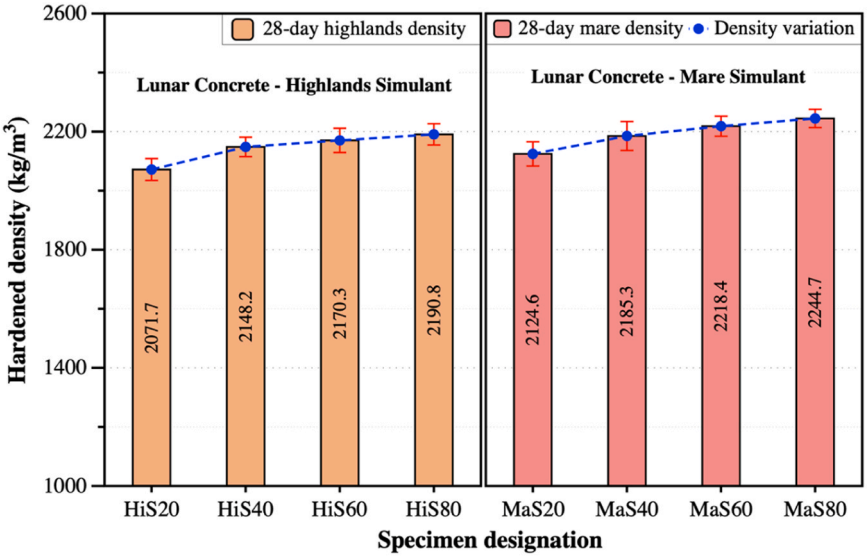

Fig. 6. Effect of regolith simulant addition on unit weight of LHSC.

was observed where the strength increased with the curing time, which was emblematic of the progressive hydration and densification process within binder materials. Notably, the LC-HiS40 and LC-MaS40 samples demonstrated the highest strength values of all tested ages within their own categories, approaching 106.7 and 98.7 MPa at 28 days, respectively. Interestingly, the compressive strength of both lunar geopolymers initially enhanced and then diminished as the simulant content increased, with the most pronounced decline occurring at a simulant introduction of 80 %. As an illustration, the 28-day strength for LHS-1-derived LHSC improved from 92.4 MPa to 106.7 MPa (increased by 15.5 %) when the simulant mass addition was raised from 20 % to 40 %. However, further increase in simulant addition to 60 % and 80 % led to

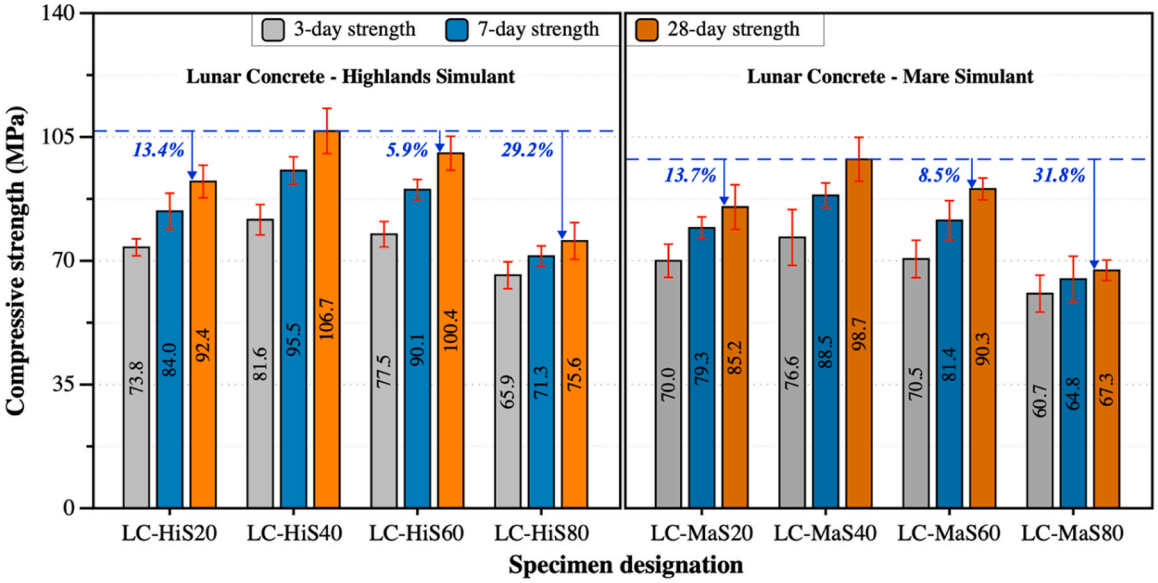

Fig. 7. Compressive strength of LHSC with different percentages of lunar simulant addition.

diminishment to 100.4 MPa (reduced by 5.9 %) and 75.6 MPa (reduced by 29.2 %), respectively. The primary cause of this phenomenon was attributed to the constant alkali activator solution (AAS) content while increasing the mass ratio with GGBS, fly ash, and silica fume [40]. As listed in Table 2, these materials were rich in CaO, SiO_2, and Al_2O_3, and their enhanced mass ratios contributed to a denser 3D polymeric framework. The high reactivity of GGBS was responsible for an exothermic reaction during its alkaline dissolution, with the resultant heat release promoting the polymerization of other precursor materials [41,42]. Moreover, the substantial presence of Ca^{2+} within GGBS was instrumental in the synthesis for hydrating products, especially calcium silicate (C-S-H) gel, which could provide the nucleation sites that promoted the formation of the calcium aluminosilicate (C-A-S-H) and sodium aluminosilicate (N-A-S-H) gels with high density and mechanical robustness [40]. Consequently, the volume of the hydrating products increased, leading to an enhanced compressive strength of LHSC. However, an overplus of Ca^{2+} (for the samples HiS20 and MaS20) reduced the likelihood of interaction among reactive molecules, thereby inhibiting the continuous formation of these gels due to the decreased solubility of silica-aluminium compounds, which ultimately reduced the strength of lunar geopolymers [43]. In cases where the simulants constituted to 80 % of the total binders (LC-HiS80 and LC-MaS80), the marked decline in compressive strength was likely due to an increased pH level in the mixture resulted from the simulants acting dual roles as both precursors and aggregates. The higher pH promoted the passivation of alkali metal ions on the surfaces of the precursors, leading to the development of the reaction products that coated the unreacted particles. Such coating hindered the dissolution of the precursors, thus reducing the formation of hydration products such as C-S-H, C-A-S-H, and N-A-S-H gels. It is noteworthy that under the same simulant content conditions, LHS-1-derived LHSC exhibited superior compressive strength than their LMS-1 counterparts at all testing ages. Moreover, the impact of varying simulant content on strength was more evident. For example, increasing the LMS-1 mass ratio from 40 % to 80 % led to a reduction in the 28-day strength by 8.5 % and 31.8 %, which was crucial for gel formation in geopolymerization and the development of the ultimate strength. Furthermore, a relatively high Si/Al ratio of 3.78 in LMS-1 led to an inadequate presence of Al atom to partake effectively in the geopolymerization - a critical process where Al could potentially substitute Si in the Si-O framework, therefore forming the corner-sharing oxygen bridges with adjacent Si atoms [44]. Consequently, to optimize factors such as flowability, compressive strength, and suitability for ISRU in lunar conditions, a simulant addition of 60 % by mass was identified as the most advantageous for the fabrication of LHSC.

3.3.2. *Modulus of elasticity*

The modulus of elasticity (MOE) of concrete signifies the material's inherent capacity to withstand elastic deformation when subjected to external forces, which is crucial for the analysis of structural design and the evaluation of concrete performance. Fig. 8(a) presents the variation in 28-day MOE for LHSC with varying proportions of LHS-1 and LMS-1. The values represented were the average of triplicate cubic sample measurements obtained from compressive tests. These were determined via dividing the stress by the corresponding longitudinal strain as captured and recorded by DIC apparatus. It was observed that the MOE for both types of lunar geopolymers initially increased but subsequently diminished with an increase in simulant addition. The peak MOE was recorded at 36.8 GPa for LC-HiS40 and 34.3 GPa for LC-MaS40 samples. When the simulant content increased to 80 %, the MOE decreased from 36.8 to 30.3 GPa (LC-HiS80) with a reduction of 17.7 %, and from 34.3 to 28.7 GPa (LC-MaS80) with a reduction of 16.3 %. Consequently, the addition of a substantial amount of soil simulant markedly weakened the capacity of LHSC to resist the elastic deformation. This effect was likely attributed to the MOE being derived from the elastic part of the compressive stress-strain relationship of samples, where the MOE generally varied in response to changes in its compressive strength. Fig. 8(b) depicts the correlation between the 28-day compressive strength and the MOE of LHSC, excluding the influence of different types of lunar regolith simulants. The figure showed that an increase in compressive strength (f_c, ranging from 65 MPa and 110 MPa) led to a proportional enhancement of MOE. A strong relationship was apparent between these two variables, as evidenced by the regression equation $MOE = 3708 \cdot f_c^{0.5} - 2022$ ($R^2 = 0.973$) with f_c expressed in MPa, indicating a high degree of predictability. Moreover, the MOE of LHS-1-based LHSC samples generally surpassed the fitting curve, whereas LMS-1 counterparts typically fell below it, suggesting that LMS-1-based LHSC exhibited a poorer resistance to elastic deformation as compared to LHS-1 cases.

3.3.3. *Failure patterns*

Fig. 9 illustrates the quintessential compressive failure patterns of the cubic LHSC samples infused with varying mass additions of LHS-1 and LMS-1. As clearly observed, both types of LHSC samples

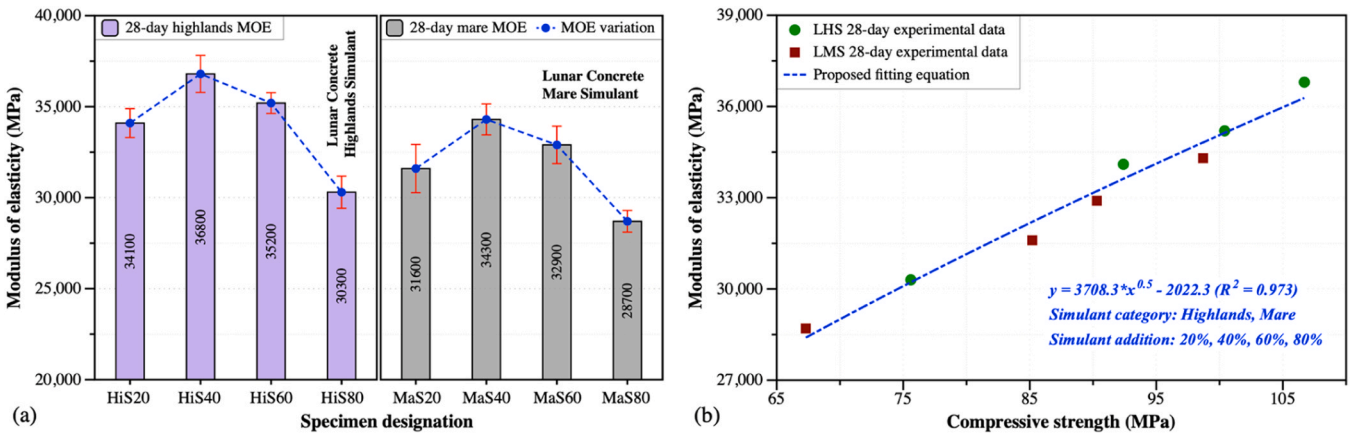

Fig. 8. (a) 28-day static MOE and (b) its correlation with compressive strength of LHSC.

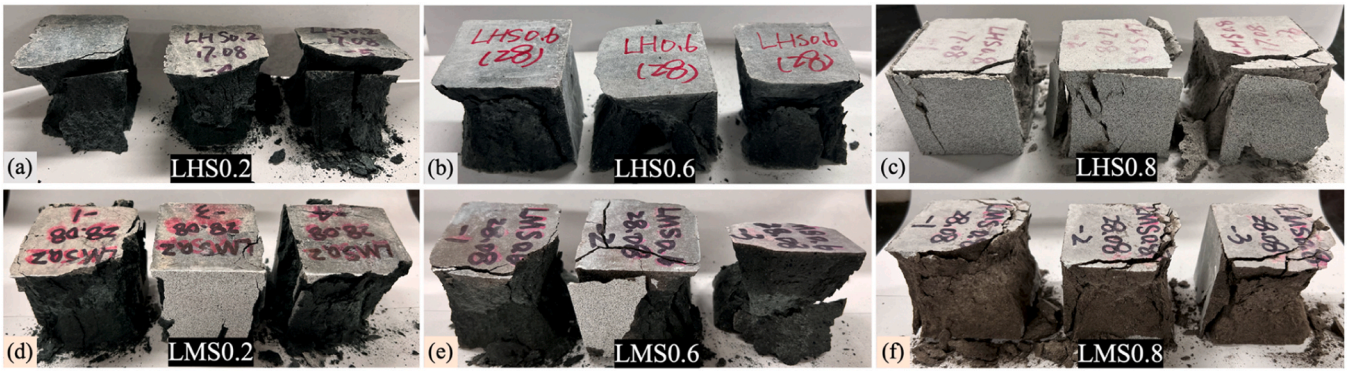

Fig. 9. Typical failure patterns of LHSC incorporating various contents of (a-c) LHS-1 and (d-f) LMS-1.

predominantly exhibited the failure mode of the conical fracturing. This was mainly characterized by the development of pyramid-shaped failure zones that originated at the corners/edges of the cubes and converged towards the central region. Such patterns suggested a compression-shear-dominated failure mechanism, where the material's brittleness was evidenced by the propagation of fractures from points of heightened stress concentration. Notably, the LHSC samples with simulant additions up to 60 % (Fig. 9(a-b and d-e)) exhibited more pronounced brittle failures, discernible by significant matrix spalling near the fracture zones. This contrasts with samples containing 80 % simulant (Fig. 9(c and f)), which displayed less severe matrix damage. This divergence in failure morphology can be attributed to the deformation behaviour of the testing machine during the loading phase. Samples with higher strength (as presented in Fig. 7) compelled the testing machine to accumulate a greater amount of elastic strain energy. When these samples approached the ultimate load-bearing capacity, the stored energy was rapidly released, resulting in the forceful crushing of the samples and a more severe matrix spalling event.

The typical evolution of vertical strain in a cubic LHSC sample subjected to compressive loading is delineated in Fig. 10. The sequence of DIC strain maps captured the dynamic responses of the test concrete at incremental loading phases. At the outset, corresponding to 15 % of the peak load (P_{max}), the strain distribution was relatively homogeneous, signalling the elastic deformation regime where microstructural damage was presumably negligible. With the load increased to 50 % of P_{max}, a more heterogeneous strain pattern emerged, indicative of the initiation of microcracking in the concrete matrix. As the compressive load increased to 85 % of P_{max}, there were evident concentrations of the strain close to the incipient failure plane, highlighting the progression towards plastic deformation and imminent macroscopic fracturing (as indicated in dotted lines). At the phase of P_{max}, the strain field revealed a critical deformation state, characterized by a distinctly demarcated shear fracture plane, which denoted the juncture of mechanical failure for LHSC sample. Finally, the post-failure image captured at 70 % of P_{max} (within the softening part) displayed significant strain concentrations along the fracture contours, with the extensive spalling of concrete matrix preventing the continuous acquisition of surface strain distribution.

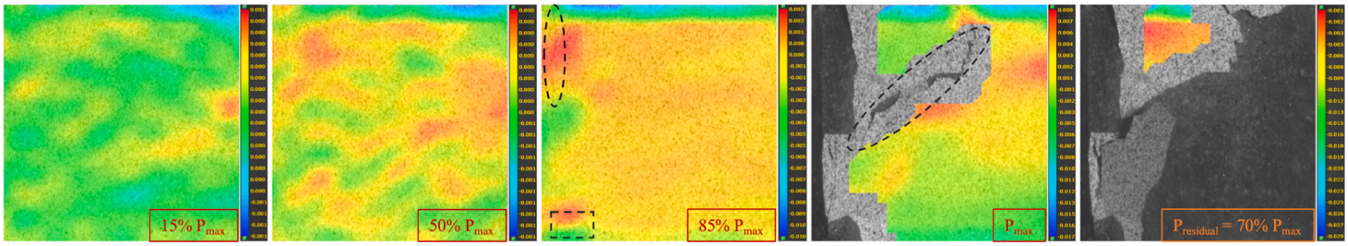

Fig. 10. Typical evolution of vertical strain field in the LHSC sample at different loading levels.

3.4. Microstructure morphology

3.4.1. Scanning electron microscopy analysis

The SEM images of the prepared LHSC formulated with varying levels of LHS-1 are displayed in Fig. 11. The images excluding the LC-HiS80 mix showed a densification in microstructure across the other compositions. At a 20 % inclusion of highlands simulant (Fig. 11(a)), the alkali activator was insufficient to completely trigger geopolymerization in all precursors, leaving behind numerous unreacted fly ash particles and immature amorphous gels within the geopolymer matrix. When the simulant addition reached 40 % (Fig. 11(b)), a noticeable decline in the count of unreacted fly ash particles occurred alongside a reduction in the number and dimensions of microcracks. Concurrently, the growth of the dense amorphous gels enhanced the compactness of the microstructure, which was reflected in the highest compressive strength of mixtures. At a simulant addition of 60 % (Fig. 11(c)), unreacted angular LHS-1 particles became evident, with an uptick in both the size and the frequency of the microcracks observed. However, when elevating the LHS-1 content to 80 % (Fig. 11(d)), the matrix exhibited greater heterogeneity, characterized by increased amount of the voids, microcracks, and unreacted simulant particles, probably owing to the aluminosilicate precipitation resulting from a reduced precursor availability and a higher alkali concentration [45]. In addition, it is noteworthy that the microstructure patterns of the foregoing mixes were distinguished by the presence of C-S-H gels, a result of the GGBS activation, which subsequently reacted with fly ash and lunar simulant. The combination of high levels of calcium, alumina, and silicate sourced from GGBS, fly ash, silica fume, and LHS-1 culminated in the formation of (N)C-A-S-H gels, markedly improving the overall performance for the derived LHSC.

Fig. 12 displays the SEM images of the LHSC composites with varying LMS-1 concentrations. The 40 % and 60 % LMS-1 mixtures (Fig. 12(b-c)) exhibited occasional and minor cracks, which did not compromise the overall microstructural compactness with a high degree of the geopolymerization. Conversely, the 20 % LMS-1 blend (Fig. 12(a)) exhibited a less compact matrix with more frequent voids and cracks, attributed to an inadequate geopolymerization from lower NaOH concentrations that resulted in amorphous gels not forming a cohesive whole. Furthermore, the mix containing 80 % LMS-1 (Fig. 12(d)) displayed significantly less compactness, with widespread and severe cracking, corresponding to the lowest compressive strength reported in Section 3.3. A comparative analysis of SEM micrographs of different lunar regolith simulant mixes revealed that the LHS-1 composites, even with equivalent mass additions, demonstrated greater structural compactness than the LMS-1 counterparts, with denser amorphous gels and fewer cracks and unreacted simulant particles. This is likely due to the higher calcium content in the LHS-1, which balances the negative charges associated with $Al(OH)_4^-$ in its derived composites, therefore leaving more Na^+ ions free in the reaction system to accelerate the geopolymerization process, as discussed in the literature [44]. It is noteworthy that unlike other research on lunar geopolymers [32,44], the prismatic-shaped side reaction products that typically degraded the mechanical performance were not observed in the microstructure of LHSC developed herein. This absence likely contributed to the notable enhancement in mechanical strength of the synthesized LHSC at similar curing temperatures.

Fig. 13 illustrates the microstructure of the LHSC, highlighting the characteristic geopolymerization process of fly ash. During the initial reaction phase (Phase I), several fly ash particles retained their distinctive microsphere shape, establishing physical connections within the geopolymer matrix. In addition, the surfaces of these fly ash particles were observed to be coated with non-reacted lunar regolith simulants. Research suggested that these unreacted fly ash particles contributed not merely as fillers but enhanced the matrix's strength over time owing to the enhanced bonding strength that developed from complex reactions

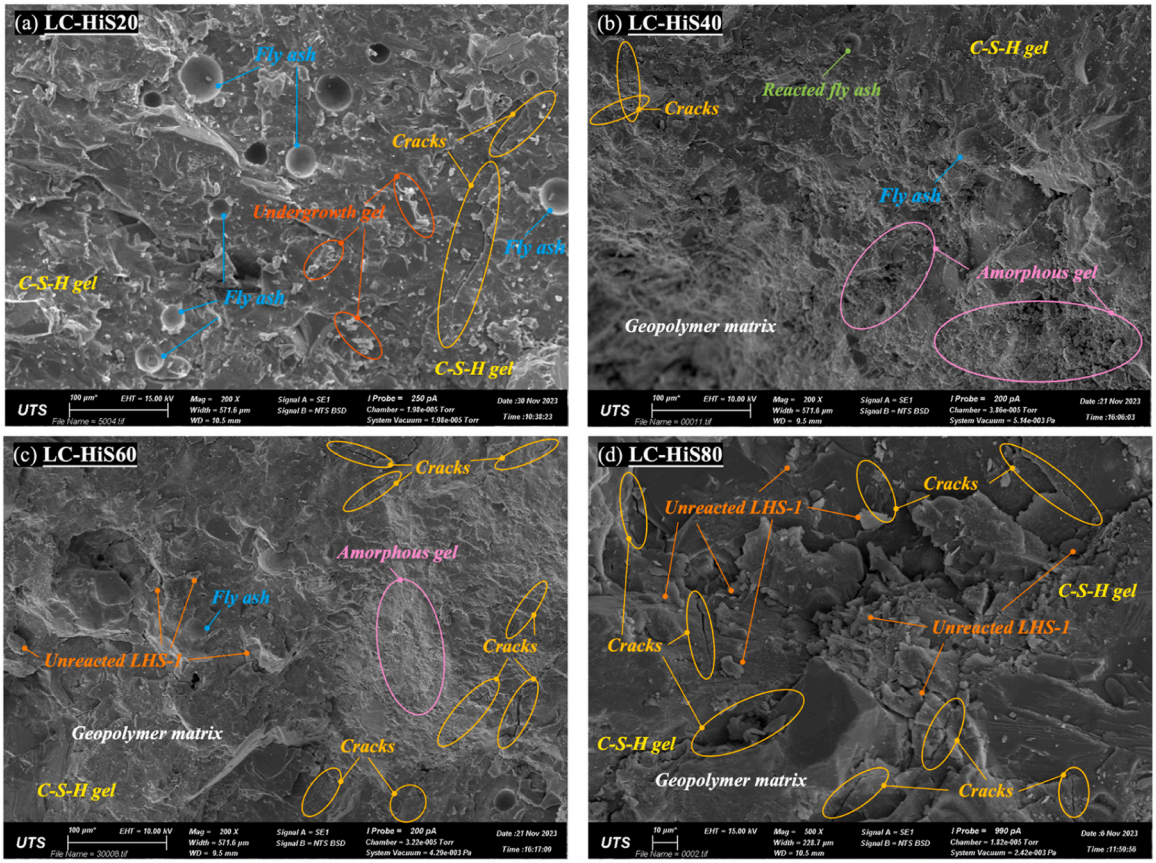

Fig. 11. SEM micrographs of LHSC incorporating (a) 20 %, (b) 40 %, (c) 60 %, and (d) 80 % of LHS-1.

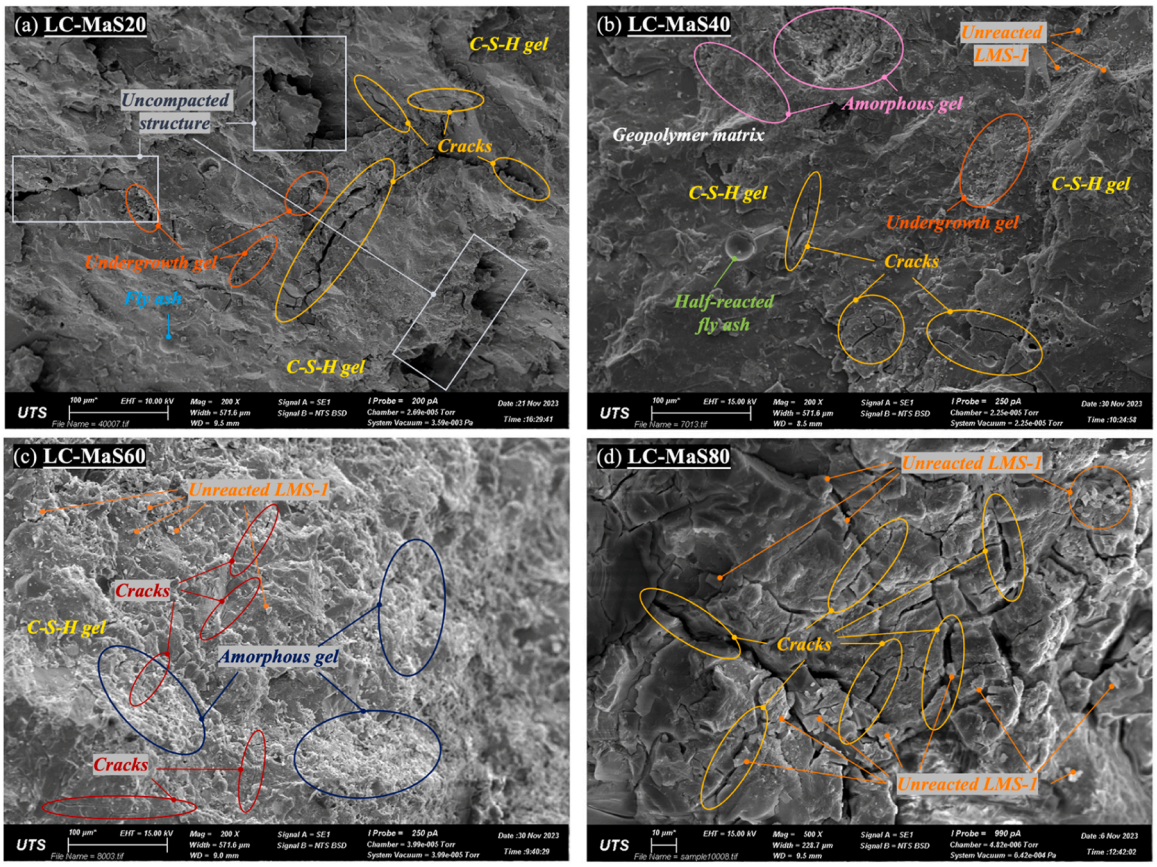

Fig. 12. SEM micrographs of LHSC incorporating (a) 20 %, (b) 40 %, (c) 60 %, and (d) 80 % of LMS-1.

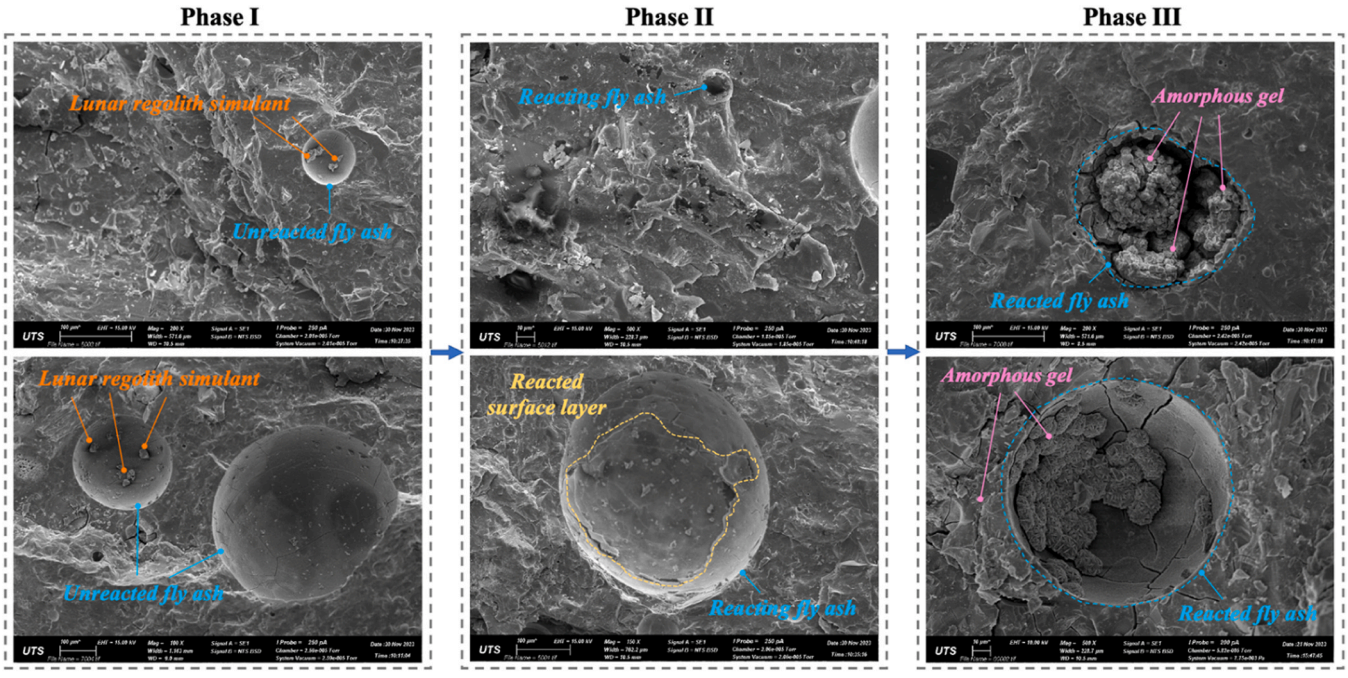

Fig. 13. Typical SEM images of fly ash microspheres in LHSC during geopolymerization.

at the particle surfaces [46]. As the process entered Phase II, the fly ash began to respond chemically, with specific areas in its vitreous matrix initiating dissolution due to the influence of alkali activation (OH^-). This reaction led to the synthesis of aluminosilicate oligomers on vitreous surfaces. Notably, the fly ash of smaller size exhibited a faster reaction rate, as evidenced by a more extensive area of dissolution on their surfaces. As the reaction progressed to Phase III, the aluminosilicate oligomers gradually evolved into an aluminosilicate gel phase. The gels

partially filled the gaps between the fly ash particles and enveloped the unreacted components, thus hindering any further reactions [47]. The lower right figure illustrated that the gels, formed by the geopolymerization of regolith simulants, neatly accumulated in the circular voids left by the fully reacted fly ash particles. Encircling these was amorphous gels produced by the geopolymerization of other precursor materials.

3.4.2. Energy dispersive spectroscopy analysis

Fig. 14 presents the EDS spectra for LHSC samples with different LHS-1 concentrations, illustrating the elemental composition of the gel products. The spectra consistently revealed the major presence of Ca, Si, Al, Na, and Mg, supporting the development of the sodium aluminosilicate structure in the geopolymer matrix [48]. Specifically, Fig. 14(a) indicates that adding 20 % highlands simulant to lunar geopolymers resulted in Ca and Si being the major elements, with atomic percentages of 58.2 % and 20.3 %, respectively. The lower signal intensity of Na and Al implied that the identified region consisted mostly of C-S-H gels, with a lesser occurrence of C-A-S-H and N-A-S-H gels. At a 40 % simulant level, as shown in Fig. 14(b), while Si and Ca continued to be the dominant elements, Na and Al concentrations increased evidently, to 7.1 % and 10.8 %, respectively. This indicated a better solubility of the precursors, i.e., LHS-1, GGBS, fly ash, and silica fume, in alkaline environments, which was conductive to the generation of denser, mechanically enhanced C-A-S-H and N-A-S-H gels with more stable structures. Consequently, the concrete exhibited improved microstructural densification, as illustrated in Fig. 11(b), and the highest compressive strength, as shown in Fig. 7. When the simulant addition reached 60 % (Fig. 14(c)), the contents of Ca, Si, and Al diminished due to the significantly reduced incorporation of GGBS, fly ash, and silica fume. This led to a decreased occurrence of amorphous gels in the geopolymer, producing a less polymerized matrix. It should be pointed out that the high Mg content in this scanning region was instrumental in the formation of a new gel phase, labelled as (N)C-A-M-S-H gel, corroborated by subsequent XRD analysis. With an 80 % simulant addition, as illustrated in Fig. 14(d), the concentration levels of Si, Al, and Na were comparable to the 60 % condition, but there was a significant drop in the Ca content (now only 7.6 % atomic mass percentage). This reduction in Ca indicated a major decline in C-S-H gel production, inadequate for nucleating a dense Si-Al tetrahedral framework within the geopolymer matrix, which resulted in a marked attenuation in mechanical strength.

Fig. 15 exhibits the EDS spectra for LHSC samples that incorporated four different mass contents of LMS-1. In a manner consistent with LHS-1 samples, the main elements identified in geopolymers made of the mare simulant included Ca, Si, Al, Na, and Mg. The spectra at a 20 % LMS-1 inclusion, as depicted in Fig. 15(a), indicated that Ca and Si predominated in the detected area, with Al, Mg, and Na also presented in significant amounts. It is noteworthy that the spectra exhibited an evidently reduced signal intensity for Ca and Al, and an enhanced index for Mg, as compared to the composites with 20 % inclusion of LHS-1

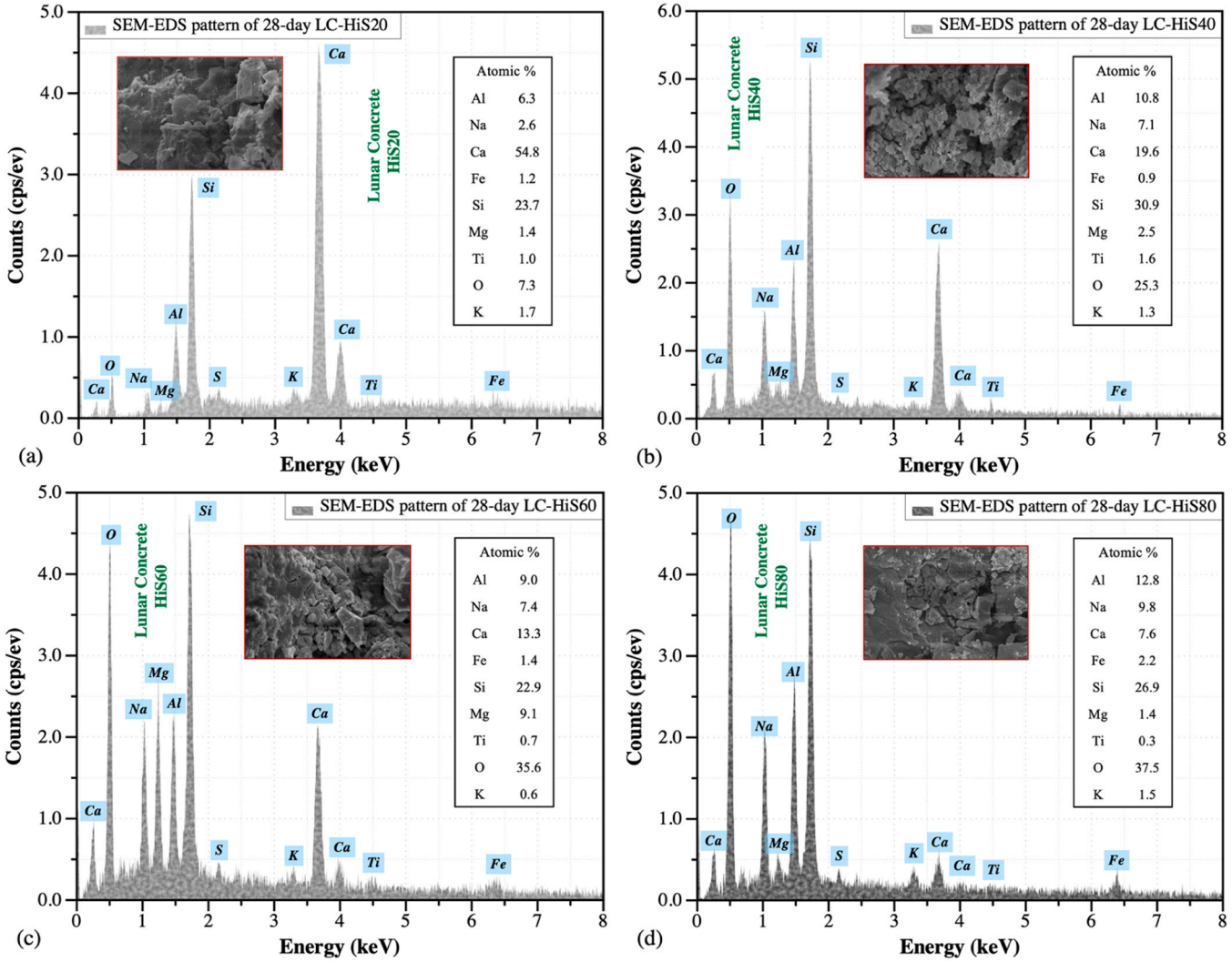

Fig. 14. SEM-EDS analysis of LHSC incorporating (a) 20 %, (b) 40 %, (c) 60 %, and (d) 80 % of LHS-1.

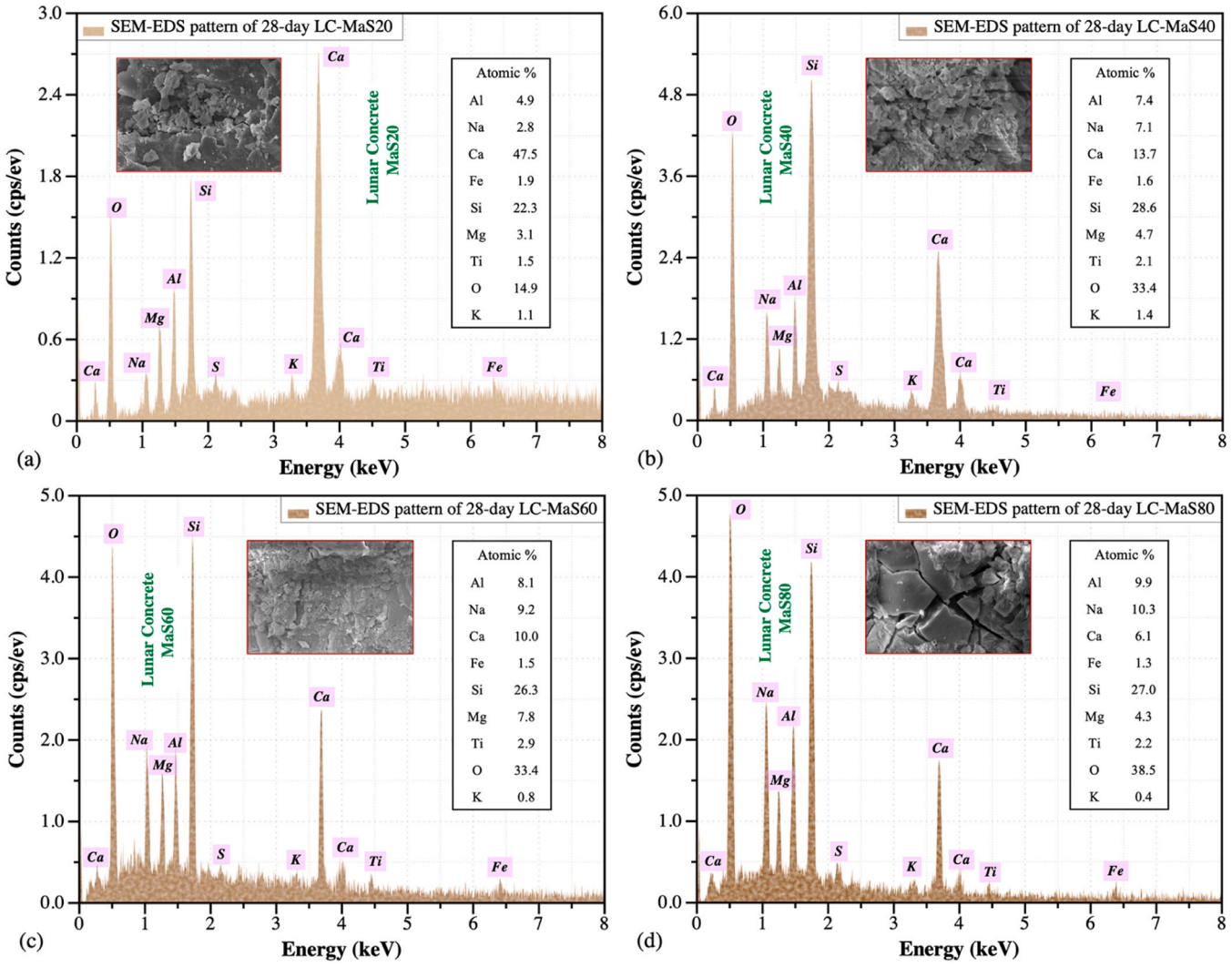

Fig. 15. SEM-EDS analysis of LHSC incorporating (a) 20 %, (b) 40 %, (c) 60 %, and (d) 80 % of LMS-1.

(referred to Fig. 14(a)). This is likely owning to the lower Al_2O_3 and CaO contents in LMS-1 and its higher MgO concentration, as listed in Table 1. Consequently, there was a decrease in gelling products including C-S-H and (N)C-A-S-H, and an increase in (N)C-A-M-S-H. As the content level of LMS-1 increased to 40 % and 60 % (Fig. 15(b-c)), the Ca content reduced owing to the diminishing mass ratio of GGBS with high CaO content, while signal intensities of Si, Na, Al, and Mg progressively intensified. This suggested that more C-S-H, (N)C-A-S-H, and (N)C-A-M-S-H gels formed, leading to an optimized microstructural densification of the matrix. Therefore, the lunar concrete prepared under these

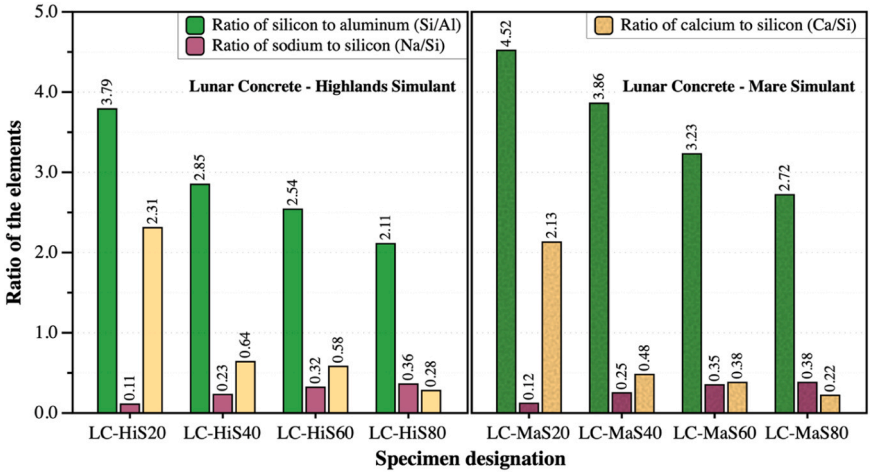

Fig. 16. Ratios of silicon, aluminium, sodium, and calcium elements detected by SEM-EDS on LHSC with different percentages of lunar simulant addition.

conditions exhibited improved strength at the macro level. However, when the LMS-1 mass ratio reached 80 %, represented in Fig. 15(d), despite the continued increase in signal intensity of Al and Na, there was a notable decrease in Ca concentration. This led to a marked decrease in C-S-H formation, which was inadequate to support the nucleated formation of (N)C-A-S-H and (N)C-A-M-S-H gels, resulting in a deteriorated microstructure and low strength. In addition, all lunar concrete samples were detected to contain a certain amount of Fe, which was believed to contribute to the formation of a glass phase that aided in the dissolution of Si, Al, and Ca and the creation of hydrated gel products [49].

Fig. 16 presents the ratios of Si, Al, Na, and Ca detected by the SEM-EDS in the synthesized LHSC, aiding in the analysis of the reaction processes and the assessment of product quality. Notably, the Si/Al ratio in two lunar concrete samples decreased with increased simulant proportions, especially when the content was raised from 20 % to 40 %, dropping from 3.79 to 2.85 for LHS-1 concrete and from 4.52 to 3.86 for LMS-1 concrete. This observed trend likely resulted from the relatively lower Si and higher Al contents in regolith simulants relative to other precursors such as GGBS, fly ash, and silica fume. A reduced Si/Al ratio suggested more Al dissolving in the alkaline solution, which caused more Si substitution in the Si-O group, leading to a higher degree of the polymerization and a more integrated Si-Al tetrahedral structure [7,50]. However, this observation deviated from the findings reported in the literatures [32,51], as the LHSC developed in this study did not consistently exhibit increased strength with a decreasing Si/Al ratio (the highest strength was observed at 40 % simulant addition, followed sequentially by 60 %, 20 %, and 80 %). This discrepancy was primarily attributed to two concurrent factors: an increase in the Na/Si ratio (from 0.11 to 0.36 in LHS-1 and from 0.12 to 0.38 in LMS-1, denoted by purple) and a decrease in the Ca/Si ratio (from 2.31 to 0.28 in LHS-1 and from 2.13 to 0.22 in LMS-1, highlighted in yellow) as the simulant addition increased from 20 % to 80 %. Optimal levels of Ca^{2+} and Na^{+} were crucial in neutralizing the negative charge from Al^{3+} dissociation, promoting the formation of abundant C-S-H, C-A-S-H, and N-A-S-H gels in the geopolymer matrix. Conversely, excessive Ca (at 20 % simulant inclusion) hastened the setting time of the mixture, causing rapid product formation that coated reactant surfaces, impeding further polymerization reaction. Meanwhile, higher Na concentrations (at 80 % simulant addition) increased the moisture content in the whole reaction system, hence reducing the ion solubility. It is noteworthy that LHS-1 cases invariably exhibited the lower Si/Al and higher Ca/Si ratios as compared to those observed in LMS-1 cases. This disparity lent substantial corroborative evidence towards elucidating the phenomenon wherein the compressive strength of LHS-1-derived LHSC consistently exceeded that of LMS-1 counterparts when subjected to equivalent mass additions.

3.4.3. X-ray diffractometry analysis

Fig. 17 exhibits the XRD patterns of LHSC samples containing varying mass additions of LHS-1. These patterns highlighted the primary

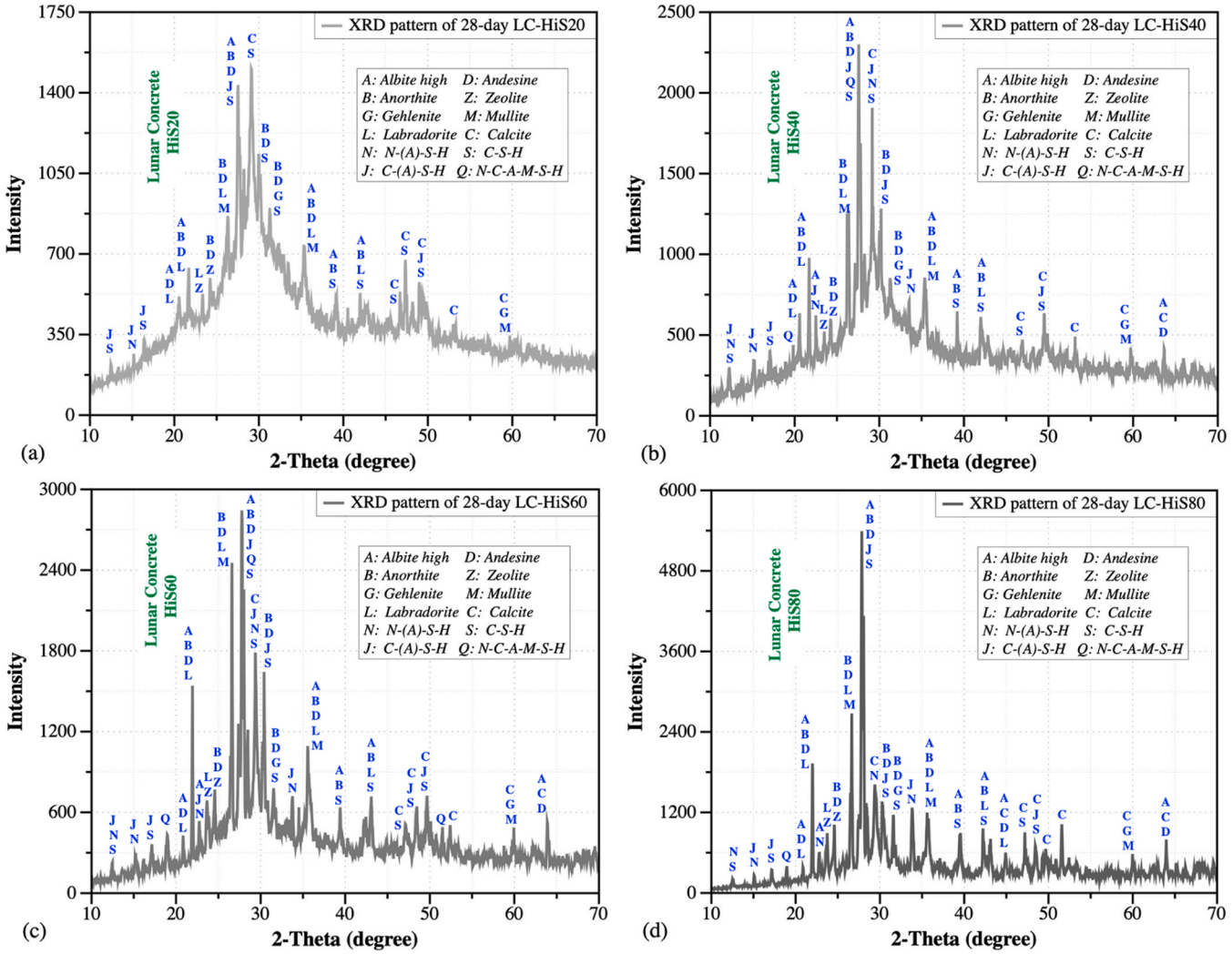

Fig. 17. XRD patterns of LHSC incorporating (a) 20 %, (b) 40 %, (c) 60 %, and (d) 80 % of LHS-1.

mineralogical phases and their relative proportions in the lunar concrete matrix, offering insight into the crystalline structures responsible for the mechanical properties. It is noticeable that the 2-theta positions of the diffraction peaks for LHS-1-synthesized lunar concrete were consistent, with the predominant phases identified as amorphous gels, anorthite, andesine, mullite, albite, and calcite. The presence of C-S-H gel was evident in all concrete samples prior to the formation of C-A-S-H and N-A-S-H gels. The Ca from the C-S-H gel accelerated the dissolution of Si and Al from the precursor materials, with an increasing consumption of Ca during the curing process. In addition, (N)C-A-M-S-H gel phases were detected in samples with 40 % and 60 % LHS-1 at 2-theta of 20.55°, 27.58°, and 51.23°, as depicted in Fig. 17(b-c). This indicated that the coexisting four gels contributed to the densification of the resulting lunar geopolymer concrete. At a 20 % LHS-1 addition (Fig. 17(a)), the primary gel phase identified was C-S-H, which aligned with the ESD patterns observed for the same sample. However, upon raising the simulant addition to 80 % (Fig. 17(d)), there was a notable attenuation in the diffraction intensity of the gel phase, and the background noise was comparatively less pronounced than in conditions with lower simulant additions. This trend indicated a reduced reactivity of precursors involved in the geopolymerization reaction and a consequent decrease in concrete strength. It should be noted that the diffraction peak at 27.58°, corresponding to the spectral peak of anorthosite in LHS-1 [8], intensified with increased LHS-1 content, illustrating a rise in inactive components acting as void fillers within the matrix. In addition, the calcite phase, detected at 2-theta positions of 19.83°, 29.18°, and 51.23°, served as an inert filler, enhancing the particle packing densification. The observation aligned with the findings by Debbarma et al. [44] and affirmed the dual function of precursors and aggregates in lunar regolith simulants, as outlined in Section 2.1.

Fig. 18 illustrates the XRD patterns for LHSC samples incorporating various contents of LMS-1. Analogous to the variations in the LHS-1 counterparts, samples with 20–60 % LMS-1 (Fig. 18(a-c)) exhibited noticeable background noise and an increased diffraction peak from amorphous gels. In addition, the fraction of inactive particles serving as void fillers within the matrix was prominently reduced in contrast with the 80 % LMS-1 cases (Fig. 18(d)). This indicated that at simulant content below 60 %, the geopolymerization of precursor materials (LMS-1, GGBS, fly ash, and silica fume) in an alkali environment reached relative completion. Concurrently, the inactive simulant particles contributed effectively to the matrix as aggregate components, synergizing with various hydration products to enhance the structural integrity. However, when LMS-1 content exceeded 60 %, the raw materials showed a reduced active-to-precursor component ratio, leading to an enhanced aggregate phase (including albite, andesine, and anorthite), as indicated by an evident increase in hump peak intensity at 27.58°. Additionally, excessive LMS-1 resulted in elevated alkali concentrations in the reaction system, facilitating the carbonation of the alkali solution with atmospheric CO_2, therefore diminishing system alkalinity and delaying the geopolymerization process. This phenomenon was also applicable to

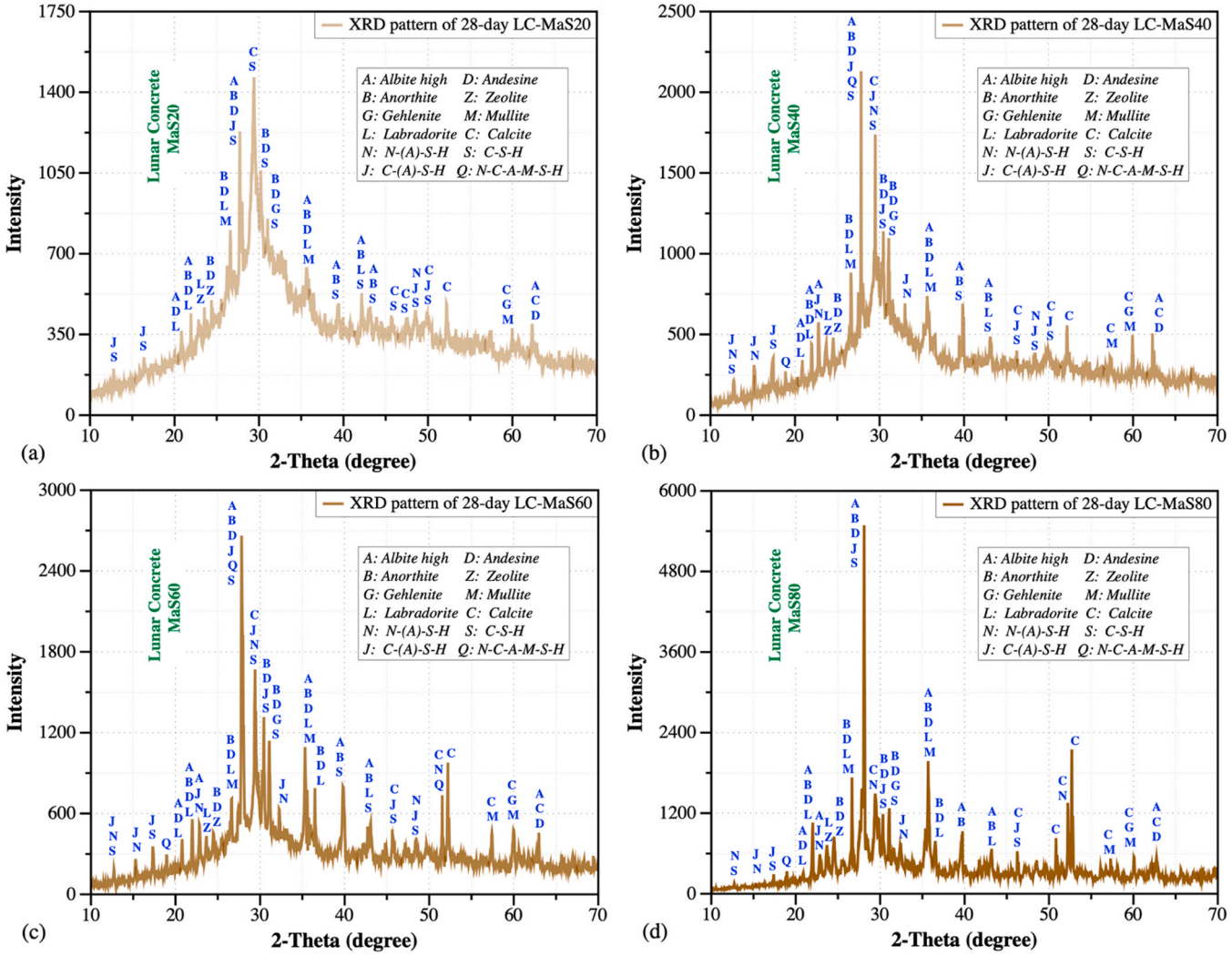

Fig. 18. XRD patterns of LHSC incorporating (a) 20 %, (b) 40 %, (c) 60 %, and (d) 80 % of LMS-1.

lunar concrete produced with LHS-1. When compared to LHS-1-derived LHSC with the same simulant dosages, the LMS-1 counterparts exhibited a lower hump peak intensity for amorphous gel phases at corresponding 2-theta positions, and a higher diffraction intensity of calcite, elucidating the inferior compressive properties from a mineralogical phase standpoint. It should be highlighted that a zeolite phase (primarily consisting of SiO_2, Al_2O_3, and Na_2O) was also present at 2-theta positions between 20° and 25°, with its hump peak being more pronounced at an 80 % simulant addition. Provis et al. [52] suggested that the formation of the zeolite phase was evidently influenced by the temperature of the system and the Si/Al ratio of raw materials. As the reaction system evolved, the amorphous gel may also convert into the zeolite phase. Zhang et al. [32] have observed that the zeolite phase, characterized by a smooth surface and distinct microcracks, could be interconnected. The presence of microcracks within the interfacial transition zones (ITZs) between the zeolite phase and amorphous gels may also contribute to the reduced mechanical strength of lunar concrete with higher regolith simulant incorporation levels.

3.5. Mass-strength efficiency

In developing lunar concrete, minimizing the transport mass of materials from Earth is crucial owing to the high costs associated with space transportation. This section uses the concept of "mass-strength efficiency", as firstly proposed by Zhou et al. [51], to evaluate the mass savings achievable with the synthesized LHSC. The mass-strength efficiency is defined by the equation:

$$\eta_{LHSC} = [(m_{GGBS} + m_{silica\ fume} + m_{fly\ ash} + m_{AAS}) \times 100 / (m_{simulant} + m_{water}) \times f_c]^{-1}$$

where η_{LHSC} denotes the mass-strength efficiency in MPa, m_x denotes the mass ratio of various raw materials (detailed in Table 3), and f_c represents the compressive strength of LHSC in MPa. Fig. 19 illustrates the variations in η_{LHSC} with different mass additions of LHS-1 and LMS-1. Results showed a significant enhancement in η_{LHSC} with both the curing age and the simulant content. For instance, for LHS-1 derived geopolymers, the efficiency values rose from 0.204 to 1.394 MPa as the simulant addition increased from 20 % to 80 %. Similarly, for LMS-1, the values increased from 0.188 to 1.241 MPa. The potential cost reductions, comparing LC-HiS80 with LC-HiS20, and LC-MaS80 with LC-MaS20, suggest savings of 418.5 % and 451.3 %, respectively, when the unit mass of Moon-sourced materials is converted into 1.0 MPa of compressive strength. Notably, the initial curing period reveals an evident increase in efficiency from 40 % to 60 % and then to 80 % simulant content. Specifically, the η_{LHSC} for LHS-1 improved by 82.6 % and 61.1 % within 3 days, while LMS-1 exhibited gains of 76.8 % and 63.1 %. At the 28-day period, these increases mitigated to 80.9 % and 42.7 % for LHS-1, and 76.1 % and 41.2 % for LMS-1, respectively. These findings underscore the crucial role of higher simulant additions in enhancing mass saving effects during the early construction phases under the challenging lunar conditions. Nevertheless, it can also be noted from the above comparisons that the diminishing evidently returned on η_{LHSC} when simulant content exceeded 60 %, owing to a marked reduction in compressive strength of LHSC at higher simulant levels.

4. Conclusion and future work

This research examines the practicality of synthesizing cement-free LHSC by utilizing two simulants of lunar regolith, LHS-1 and LMS-1. Samples were cured at temperatures typical of the lunar surface to mimic conditions found at a 30-degree lunar altitude. The optimum mass ratio for combining the regolith simulant with precursors was identified, leading to an in-depth analysis of the compression and microstructure of the geopolymers formed. Given the outcomes of this research, the following conclusions can be drawn:

1) The LMS-1-derived LHSC exhibited a better flowability as compared to LHS-1 counterparts. Increasing the mass ratio of both simulants in the mix directly contributed to an elevated unit weight of the synthesized LHSC.
2) The compressive strength of the LHSC initially enhanced with the simulant content and then diminished, with peak strengths observed at 106.7 MPa for LC-HiS40 and 98.7 MPa for LC-MaS40. A proportional relationship between compressive strength and MOE was established ($MOE = 3708.3 \cdot f_c^{0.5}$ - 2022.3, $R^2 = 0.973$), suggesting a predictive model for elastic properties based on strength characteristics.
3) SEM analysis showed better structural compactness and lower presence of unreacted simulant particles in LHS-1-derived LHSC. Geopolymer gels formed by simulants were neatly located in voids left by the fully reacted fly ash particles, encircled with amorphous gels produced by the geopolymerization of other precursor materials.
4) EDS and XRD analysis revealed differences in the chemical ratios and mineralogical phases between LHS-1 and LMS-1 derived LHSC. LHS-1 samples consistently demonstrated a better performance, attributed to favourable Si/Al and Ca/Si ratios as well as a higher hump

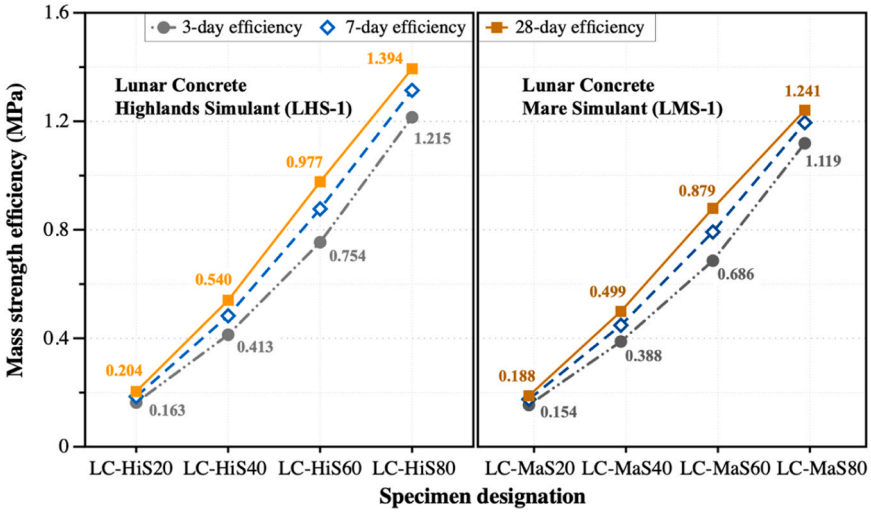

Fig. 19. Mass-strength efficiency of LHSC containing various percentages of LHS-1 and LMS-1.

intensity of amorphous gel phases and a lower diffraction peak of calcite.

5) The moderate concentrations of Ca, Na, Si, and Al were instrumental in facilitating a more complete geopolymerization reaction in LHSC. Upon evaluating the flowability, compressive strength, micromorphology, and mass-strength efficiency, a 60 % by mass addition of LHS-1 was optimum for constructing LHSC near the Apollo 17 landing site, given its suitability for ISRU in lunar environments.

The employment of lunar regolith simulants for the synthesis of geopolymers provides a promising foundation for producing robust construction materials in extra-terrestrial environments, where the traditional cement-based concrete is impractical. Future research will concentrate on incorporating various fibre materials into the geopolymer matrix to enhance its tensile strength and ductility, which were key attributes for mitigating the inherent brittleness of lunar geopolymers. Additionally, studies into the properties and durability of fibre-reinforced high/ultra-high performance lunar geopolymers will be carried out under simulated lunar conditions, including extreme temperature fluctuations and micrometeorite impacts. It is important to note that given the logistical complexities and high costs associated with transporting traditional geopolymer materials like GGBS, fly ash, silica fume, NaOH, and Na_2SiO_3 to the Moon, upcoming research will extensively investigate the synthesis of high/ultra-high performance lunar geopolymers utilizing only in-situ resources. In addition, the exploration of viable alternatives that can be sourced or synthesized directly on the Moon will be prioritised. These initiatives are integral to a fully ISRU strategy, which aims to include all necessary components such as precursors, aggregates, and alkali activators, ensuring a self-sufficient construction methodology for lunar habitats.

CRediT authorship contribution statement

Ruizhe Shao: Writing – original draft, Methodology, Investigation, Conceptualization. **Chengqing Wu:** Writing – review & editing, Visualization, Supervision, Resources, Methodology, Conceptualization. **Jun Li:** Writing – review & editing, Methodology, Conceptualization.

Declaration of Competing Interest

The authors declare that they have no known competing financial interests or personal relationships that could have appeared to influence the work reported in this paper.

Acknowledgements

The study presented herein is supported by the ARC Discovery Grant DP210101100. Thanks are due to PhD students Chaocong Wang, Junjie Huang, and Zizheng Yu for assistance with the experiments.

Data availability

Data will be made available on request.

References

[1] M. Smith, D. Craig, N. Herrmann, E. Mahoney, J. Krezel, N. McIntyre, K. Goodliff, The artemis program: an overview of NASA's activities to return humans to the moon, in: Proceedings of the IEEE Aerospace Conference, IEEE, New York, 2020.
[2] Z. Hu, T. Shi, M. Cen, J. Wang, X. Zhao, C. Zeng, Y. Zhou, Y. Fan, Y. Liu, Z. Zhao, Research progress on lunar and martian concrete, Constr. Build. Mater. 343 (2022) 128117.
[3] D. Vaniman, R. Reedy, G. Heiken, G. Olhoeft, W. Mendell, The Lunar Environment, The Lunar Sourcebook, CUP, 1991, pp. 27–60.
[4] L. Cai, L. Ding, H. Luo, X. Yi, Preparation of autoclave concrete from basaltic lunar regolith simulant: effect of mixture and manufacture process, Constr. Build. Mater. 207 (2019) 373–386.
[5] Y.C. Toklu, P. Akpinar, Lunar soils, simulants and lunar construction materials: an overview, Adv. Space Res. 70 (3) (2022) 762–779.
[6] J.N. Mills, M. Katzarova, N.J. Wagner, Comparison of lunar and martian regolith simulant-based geopolymer cements formed by alkali-activation for in-situ resource utilization, Adv. Space Res. 69 (1) (2022) 761–777.
[7] S. Zhou, Z. Yang, R. Zhang, X. Zhu, F. Li, Preparation and evaluation of geopolymer based on BH-2 lunar regolith simulant under lunar surface temperature and vacuum condition, Acta Astronaut. 189 (2021) 90–98.
[8] M. Isachenkov, S. Chugunov, Z. Landsman, I. Akhatov, A. Metke, A. Tikhonov, I. Shishkovsky, Characterization of novel lunar highland and mare simulants for ISRU research applications, Icarus 376 (2022) 114873.
[9] E. Robens, A. Dąbrowski, S. Chibowski, R. Dobrowolski, M. Drewniak, M. Dumańska-Słowik, W. Gac, J. Goworek, M. Huber, M. Iwan, Investigation of surface properties of lunar regolith - part IV, Ann. Univ. Mariae Curie Sk. Sect. AA Chem. 63 (2008) 144–168.
[10] W.D. Carrier III, Particle size distribution of lunar soil, J. Geotech. Geoenviron. Eng. 129 (10) (2003) 956–959.
[11] J.-G. Guo, T. Ying, H. Gao, X. Chen, Y. Song, T. Lin, Q. Zhang, Q. Zheng, C. Li, Y. Xu, Surface microstructures of lunar soil returned by Chang'E-5 mission reveal an intermediate stage in space weathering process, Sci. Bull. 67 (16) (2022) 1696–1701.
[12] Z. Wang, Y. Wu, D.T. Blewett, E.A. Cloutis, Y. Zheng, J. Chen, Submicroscopic metallic iron in lunar soils estimated from the in situ spectra of the Chang'E-3 mission, Geophys. Res. Lett. 44 (8) (2017) 3485–3492.
[13] P.J. Collins, J. Edmunson, M. Fiske, A. Radlińska, Materials characterization of various lunar regolith simulants for use in geopolymer lunar concrete, Adv. Space Res. 69 (11) (2022) 3941–3951.
[14] P.J. Collins, R.J. Thomas, A. Radlińska, Influence of gravity on the micromechanical properties of portland cement and lunar regolith simulant composites, Cem. Concr. Res. 172 (2023) 107232.
[15] X. Hou, T. Ding, T. Chen, Y. Liu, M. Li, Z. Deng, Constitutive properties of irregularly shaped lunar soil simulant particles, Powder Technol. 346 (2019) 137–149.
[16] H.A. Toutanji, S. Evans, R.N. Grugel, Performance of lunar sulfur concrete in lunar environments, Constr. Build. Mater. 29 (2012) 444–448.
[17] S. Gholami, X. Zhang, Y.-J. Kim, Y.-R. Kim, B. Cui, H.-S. Shin, J. Lee, Hybrid microwave sintering of a lunar soil simulant: effects of processing parameters on microstructure characteristics and mechanical properties, Mater. Des. 220 (2022) 110878.
[18] H. Kanamori, S. Udagawa, T. Yoshida, S. Matsumoto, K. Takagi, Properties of lunar soil simulant manufactured in Japan, Space 98 (1998) 462–468.
[19] Y. Zheng, S. Wang, Z. Ouyang, Y. Zou, J. Liu, C. Li, X. Li, J. Feng, CAS-1 lunar soil simulant, Adv. Space Res. 43 (3) (2009) 448–454.
[20] R. Zhang, S. Zhou, F. Li, Y. Bi, X. Zhu, Mechanical and microstructural characterization of carbon nanofiber–reinforced geopolymer nanocomposite based on lunar regolith simulant, J. Mater. Civ. Eng. 34 (1) (2022) 04021387.
[21] Y.-J. Kim, B.H. Ryu, H. Jin, J. Lee, H.-S. Shin, Microstructural, mechanical, and thermal properties of microwave-sintered KLS-1 lunar regolith simulant, Ceram. Int. 47 (19) (2021) 26891–26897.
[22] G. Xiong, X. Guo, S. Yuan, M. Xia, Z. Wang, The mechanical and structural properties of lunar regolith simulant based geopolymer under extreme temperature environment on the moon through experimental and simulation methods, Constr. Build. Mater. 325 (2022) 126679.
[23] C. Montes, K. Broussard, M. Gongre, N. Simicevic, J. Mejia, J. Tham, E. Allouche, G. Davis, Evaluation of lunar regolith geopolymer binder as a radioactive shielding material for space exploration applications, Adv. Space Res. 56 (6) (2015) 1212–1221.
[24] N. Li, C. Shi, Z. Zhang, H. Wang, Y. Liu, A review on mixture design methods for geopolymer concrete, Compos. Part B Eng. 178 (2019) 107490.
[25] W. Hu, Q. Nie, B. Huang, A. Su, Y. Du, X. Shu, Q. He, Mechanical property and microstructure characteristics of geopolymer stabilized aggregate base, Constr. Build. Mater. 191 (2018) 1120–1127.
[26] P. Zhang, X. Han, S. Hu, J. Wang, T. Wang, High-temperature behavior of polyvinyl alcohol fiber-reinforced metakaolin/fly ash-based geopolymer mortar, Compos. Part B Eng. 244 (2022) 110171.
[27] K. Wang, Q. Tang, X. Cui, Y. He, L. Liu, Development of near-zero water consumption cement materials via the geopolymerization of tektites and its implication for lunar construction, Sci. Rep. 6 (1) (2016) 29659.
[28] K. Wang, P.N. Lemougna, Q. Tang, W. Li, X. Cui, Lunar regolith can allow the synthesis of cement materials with near-zero water consumption, Gondwana Res. 44 (2017) 1–6.
[29] S. Wilhelm, M. Curbach, Review of possible mineral materials and production techniques for a building material on the moon, Struct. Concr. 15 (3) (2014) 419–428.
[30] A. Alexiadis, F. Alberini, M.E. Meyer, Geopolymers from lunar and martian soil simulants, Adv. Space Res. 59 (1) (2017) 490–495.
[31] S. Zhou, X. Zhu, C. Lu, F. Li, Synthesis and characterization of geopolymer from lunar regolith simulant based on natural volcanic scoria, Chin. J. Aeronaut. 35 (1) (2022) 144–159.
[32] R. Zhang, S. Zhou, F. Li, Preparation of geopolymer based on lunar regolith simulant at in-situ lunar temperature and its durability under lunar high and cryogenic temperature, Constr. Build. Mater. 318 (2022) 126033.
[33] A.R. Clendenen, A. Aleksandrov, B.M. Jones, P.G. Loutzenhiser, D.T. Britt, T. M. Orlando, Temperature programmed desorption comparison of lunar regolith to lunar regolith simulants LMS-1 and LHS-1, Earth Planet. Sci. Lett. 592 (2022) 117632.

[34] S. Xu, P. Yuan, J. Liu, Z. Pan, Z. Liu, Y. Su, J. Li, C. Wu, Development and preliminary mix design of ultra-high-performance concrete based on geopolymer, Constr. Build. Mater. 308 (2021) 125110.
[35] C. Li, H. Hu, M. Yang, Z. Pei, Q. Zhou, X. Ren, B. Liu, D. Liu, X. Zeng, G. Zhang, Characteristics of the lunar samples returned by the Chang'E-5 mission, Natl. Sci. Rev. 9 (2) (2022) nwab188.
[36] ASTM C1437, Standard Test Method for Flow of Hydraulic Cement Mortar, American Society for Testing and Materials, Philadelphia, 2013.
[37] ASTM C109/C109M, Standard Test Method for Compressive Strength of Hydraulic Cement Mortars, American Society for Testing and Materials, Philadelphia, 2013.
[38] A. Rafeet, R. Vinai, M. Soutsos, W. Sha, Guidelines for mix proportioning of fly ash/GGBS based alkali activated concretes, Constr. Build. Mater. 147 (2017) 130–142.
[39] A. Dehghani, F. Aslani, N. Ghaebi Panah, Effects of initial SiO2/Al2O3 molar ratio and slag on fly ash-based ambient cured geopolymer properties, Constr. Build. Mater. 293 (2021) 123527.
[40] J. Xie, J. Wang, R. Rao, C. Wang, C. Fang, Effects of combined usage of GGBS and fly ash on workability and mechanical properties of alkali activated geopolymer concrete with recycled aggregate, Compos. Part B Eng. 164 (2019) 179–190.
[41] J.N.Y. Djobo, D. Stephan, The reaction of calcium during the formation of metakaolin phosphate geopolymer binder, Cem. Concr. Res. 158 (2022) 106840.
[42] Z. Zhang, Z. Zhou, H. Zhu, P. Duan, Y. Fang, Z. Jiang, Mechanisms of CLDH seeding on hydration kinetics of slag-based geopolymer: towards aluminosilicate cement phase engineering, Compos. Part B Eng. 271 (2024) 111157.
[43] A. Bouaissi, L. Li, M.M.A.B. Abdullah, Q.-B. Bui, Mechanical properties and microstructure analysis of FA-GGBS-HMNS based geopolymer concrete, Constr. Build. Mater. 210 (2019) 198–209.
[44] S. Debbarma, X. Shi, A. Torres, M. Nodehi, Fiber-reinforced lunar geopolymers synthesized using lunar regolith simulants, Acta Astronaut. 214 (2024) 593–608.
[45] W. Lee, J. Van Deventer, The effects of inorganic salt contamination on the strength and durability of geopolymers, Colloids Surf. A Physicochem. Eng. Asp. 211 (2-3) (2002) 115–126.
[46] G.S. Ryu, Y.B. Lee, K.T. Koh, Y.S. Chung, The mechanical properties of fly ash-based geopolymer concrete with alkaline activators, Constr. Build. Mater. 47 (2013) 409–418.
[47] F. Okoye, J. Durgaprasad, N. Singh, Effect of silica fume on the mechanical properties of fly ash based-geopolymer concrete, Ceram. Int. 42 (2) (2016) 3000–3006.
[48] R. Çetintaş, S. Soyer-Uzun, Relations between structural characteristics and compressive strength in volcanic ash based one-part geopolymer systems, J. Build. Eng. 20 (2018) 130–136.
[49] H. Sethi, P.P. Bansal, R. Sharma, Effect of addition of GGBS and glass powder on the properties of geopolymer concrete, Iran. J. Sci. Technol. Trans. Civ. Eng. 43 (2019) 607–617.
[50] M.E. Krüger, A. Heisig, H. Hilbig, H. Eickhoff, D. Heinz, A. Machner, Effect of aluminum on the structure of synthetic alkali-silica gels, Cem. Concr. Res. 166 (2023) 107088.
[51] S. Zhou, C. Lu, X. Zhu, F. Li, Preparation and characterization of high-strength geopolymer based on BH-1 lunar soil simulant with low alkali content, Engineering 7 (11) (2021) 1631–1645.
[52] J.L. Provis, G.C. Lukey, J.S. van Deventer, Do geopolymers actually contain nanocrystalline zeolites? A reexamination of existing results, Chem. Mater. 17 (12) (2005) 3075–3085.